

RESEARCH ARTICLE SUMMARY

PEROVSKITE EMITTERS

A hierarchical shell locks and stabilizes perovskite nanocrystals with near-unity quantum yield

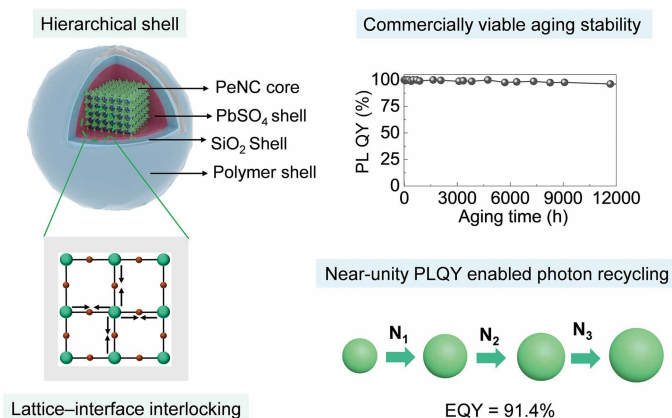
Qingsen Zeng *et al.*

Full article and list of author affiliations:
<https://doi.org/10.1126/science.ady1370>

INTRODUCTION: Luminescent materials have powered advances in various applications, including displays, lighting, sensing, imaging, and optical communication. Solid-state light emitters must exhibit both strong absorption and high photoluminescence quantum yield (PLQY) to maximize light-conversion efficiency. However, almost all known emitters exhibit concentration-induced quenching and self-absorption when integrated into dense solid films, fundamentally limiting external quantum yield (EQY; $\text{PLQY} \times \text{absorptance}$) and light-conversion efficiency. Consequently, more than 2000 terawatt-hours of electricity are wasted annually in lighting and display technologies because of suboptimal electro-optical conversion, corresponding to $\sim 8\%$ of global electricity consumption. Colloidal perovskite nanocrystals (PeNCs) possess high absorption coefficients and intrinsically high PLQY, making them promising light-conversion materials. Yet their soft ionic lattices and labile surfaces undergo light-, heat-, and moisture-induced structural and chemical degradation. Achieving near-unity PLQY with commercially viable stability remains a central challenge.

RATIONALE: Recent findings in bulk perovskites indicated that photo- or thermal-induced lattice expansion softens the crystal lattice and accelerates defect formation. However, how this lattice-softening couples with surface reactions in colloidal PeNC solids has remained unclear. We identify that PeNC degradation proceeds through a lattice-interface interlinked pathway, in which lattice expansion weakens ionic bonding, enhances ion migration, and facilitates surface oxidation and hydration reactions. Therefore, a stabilization strategy must simultaneously lock the lattice and chemically stabilize the surface rather than act only as a passive barrier.

RESULTS: We introduce a hierarchical shell (HS) composed of interbonded $\text{PbSO}_4\text{-SiO}_2\text{-siloxane}$ layers. This structure forms a lattice-interface interlocking network that locks the ionic lattice and stabilizes surface chemistry. HS inorganic PeNC (HS- CsPbBr_3) films show a time for 10% PLQY loss (T_{90}) of 3211 hours at 60°C , 90% relative humidity (RH) and 12,000 hours under continuous blue-light illumination, indicating long-term stability relevant for potential commercial applications. The HS strategy is compositionally general and scalable, enabling stable emission across 409 to 783 nm, including mixed-halide and hybrid perovskite formulations. Furthermore, HS organic-inorganic hybrid PeNC (HS- MAPbBr_3) showing pure-green emission, a composition that is typically highly vulnerable to moisture and heat, exhibits extended humid-thermal and photostability lifetimes, surpassing $T_{90} = 3900$ hours and estimated $T_{90} = 27,234$ hours, respectively. HS- MAPbBr_3 PeNC films also achieve 100.0% PLQY (average 98.6%), turning self-absorption into efficient photon recycling. A 20 wt % HS- MAPbBr_3 film achieves $\text{EQY} = 91.4\%$, approaching the theoretical limit and surpassing previously reported solid-state emitters. The HS structure prevents



A HS enables lattice-interface interlocking, transforming colloidal perovskite nanocrystals into commercially viable solid-state emitters. The interbonded $\text{PbSO}_4\text{-SiO}_2\text{-polymer}$ layers confine lattice expansion and stabilize the surface, suppressing soft-lattice-driven degradation. As a result, HS-PeNC films maintain near-unity PLQY with efficient photon recycling and achieve an external quantum yield of 91.4%, alongside commercially viable stability ($T_{90} > 3000$ hours at 60°C , 90% RH; $T_{90} > 27,000$ hours under blue-light exposure).

lead leakage and supports roll-to-roll coating, inkjet printing, and >3500 pixels per inch photolithographic patterning for high-resolution display demonstrations.

CONCLUSION: The HS provides an interbonded stabilization framework that locks the lattice and stabilizes the interface, suppressing the lattice-interface interlinked degradation pathway. This approach enables near-unity PLQY, converts reabsorption into photon recycling, and achieves photoluminescence stability compatible with commercial use. Owing to broad compositional compatibility and patterning scalability, HS-PeNCs are well-suited for large-area displays (such as 75-inch televisions), mid-size tablets (~ 10 inch), and high-resolution microdisplays for augmented- and virtual-reality systems, as well as for solid-state lighting and bio-optoelectronic modules (for example, photoplethysmography sensing). More broadly, the lattice-interface interlocking concept provides a generalizable stabilization strategy for halide perovskite materials and related optoelectronic devices. □

Corresponding author: Tae-Woo Lee (twlees@snu.ac.kr, taewlees@gmail.com) Cite this article as Q. Zeng *et al.*, *Science* 391, eady1370 (2026). DOI: 10.1126/science.ady1370.

PEROVSKITE EMITTERS

A hierarchical shell locks and stabilizes perovskite nanocrystals with near-unity quantum yield

Qingsen Zeng^{1,2}, Yue Zhao¹, Sunghee Park^{3,4}, Huanyu Zhou¹, Hyun-Joon Shim^{1,5}, Tianshu Li⁶, Jinseok Ryu¹, Min-Jun Sung¹, Xian Wei Chua^{7,8}, Eojin Yoon¹, Barney A. I. Lewis^{7,8}, Seung-Je Woo¹, Michele Forzatti⁹, Min Ju Kim¹⁰, Eun A. Kim^{10,11}, Linjie Dai^{7,8}, Jinhyeong Jang^{12,13}, Yipeng Tang¹⁴, Jin Jung Kweon^{15,16}, Hao Chen¹, Kyung Yeon Jang¹, Dong-Hyeok Kim¹, Woo Jin Jeong¹, Joo Sung Kim^{1,5}, Hyejin Lee¹, Kyueun Lim^{1,5}, Seong-Yong Cho^{10,11}, Chan Beum Park¹³, Sung Keun Lee^{15,16}, Miyoung Kim¹, Henk J. Bolink⁹, Bin Hu¹⁴, Aron Walsh⁶, Samuel D. Stranks^{7,8}, Tae-Woo Lee^{1,2,4,5,17*}

Solid-state emitters have exhibited external quantum yields (EQYs) below 65%, with no system combining unity photoluminescence quantum yield (PLQY) and commercially viable stability. These limitations are most pronounced in colloidal perovskite nanocrystals (PeNCs), given their soft ionic lattices and labile surfaces. We introduce a hierarchical shell (HS) structure comprising interbonded PbSO₄-SiO₂-polymer multilayers that simultaneously locks and stabilizes soft lattices and labile interfaces. HS-CsPbBr₃ PeNC films exhibit T_{90} (10% PLQY loss) = 3211 hours under accelerated 60°C, 90% relative humidity (RH) and T_{90} = 12,000 hours under blue-light exposure. HS strategy generalizes across PeNC compositions—including mixed-halide, mixed-cation, iodide, and hybrid PeNCs—and enables MAPbBr₃ with extended T_{90} = 3900 hours (60°C, 90% RH) and T_{90} = 27,234 hours (blue light). Moreover, HS-MAPbBr₃ films with 100.0% PLQY eliminate self-absorption losses and achieve an EQY of 91.4%, approaching the theoretical maximum. The HS barrier also prevents lead leakage for safety of large-area, high-resolution displays and bio-optoelectronics.

For nearly a century, luminescent materials have powered advances in displays, lighting, sensing, imaging, and optical communication (1–5). Many systems—ranging from rare-earth or transition-metal phosphors, organic semiconductors, and quantum dots (QDs) to emerging carbon dots, metal nanoclusters, and halide perovskites—have demonstrated photoluminescence quantum yields (PLQYs) of >90% in dilute solution or dispersions (6–14). However, such efficiencies are typically realized under low-absorbance (A), solution-phase environments, or deep-ultraviolet (UV) excitation (<300 nm), limiting their relevance for solid-state devices excited by commercial light sources (365 to 450 nm).

In practical applications, solid emitters must simultaneously exhibit strong absorption and high PLQY to maximize light-conversion efficiency, as quantified by the external quantum yield ($EQY = A \times PLQY$). This balance is fundamentally constrained by an intrinsic trade-off: As concentration increases to boost absorbance, concentration quenching

and nonradiative losses from self-absorption inevitably reduce PLQY (8–11, 15–17), limiting EQY to <65% across nearly all known solid emitters (tables S1 to S6). As a result, >2000 terawatt-hours (TWh) of electricity—~8% of global electricity consumption—is lost annually because of suboptimal electro-optical conversion in lighting and display applications (18–21). In principle, achieving 100% PLQY—so that every photon is emitted and every reabsorbed photon is reemitted—would fully mitigate self-absorption losses and allow EQY to approach its theoretical maximum.

Colloidal halide perovskite nanocrystals (PeNCs) have emerged as bright emitters with exceptional color purity, high absorption coefficient, and >95% PLQY in well-passivated solution (22–25), offering a strong potential for achieving high EQY in solids. However, environmental stressors (such as light, heat, moisture, and oxygen) easily degrade the ionic PeNCs; this reaction severely reduces the PLQY and operational lifetime (26, 27). In bulk perovskite crystals, light- or heat-induced lattice expansion and tensile strain have recently been identified as key degradation pathways that weaken ionic bonding and accelerate ion migration, phase separation, and defect formation (28–30).

Colloidal PeNCs surrounded by weakly bound ligands share this intrinsic lattice softness, but the impact of lattice softening-driven degradation in colloidal systems has been largely overlooked. Their degradation is further complicated by labile surface chemistry and direct environmental exposure (31), especially under operational conditions in which both the lattice and interface undergo dynamic evolution. We propose that degradation in colloidal PeNCs, particularly those that lack strong shell-to-lattice anchoring, is best understood as a lattice-interface interlinked process, in which lattice expansion and softening and interfacial chemical reactions at a labile surface cooperatively accelerate structural and optical deterioration. This mechanistic gap has limited the rational design of stable and efficient PeNC materials.

For practical device integration, solid-state emitters are designed to meet commercial aging benchmarks, which is typically a time for 10% PLQY loss (T_{90}) > 1000 hours under 60°C, 90% relative humidity (RH) and T_{90} > 10,000 hours under continuous blue-light irradiation (supplementary text S1). Existing stabilization strategies of PeNCs such as polymer encapsulation (32, 33), oxide shell coating (34, 35), and ligand cross-linking (36) remain fundamentally limited because they generally function as passive diffusion barriers that hinder moisture and oxygen ingress. Relying on weakly bound ammonium or carboxylate surface ligands (32–36), all of these methods offer only limited anchoring to the ionic lattice and fail to address degradation pathways that arise from lattice-interface interlinked degradation under operational stress. Therefore, these methods struggle to sustain the high PLQY of PeNC films >80% over commercially viable operational lifetimes (table S7) (32–36). Furthermore, no existing strategy is widely applicable across PeNC compositions (such as mixed-halide, organic-inorganic hybrid, mixed-cation, or iodide-rich); this limitation presents a critical challenge because these more labile formulations are particularly prone to phase separation, halide oxidation, and ion migration under operational conditions (25, 37).

We report a hierarchical shell (HS) structure—composed of an interbonded PbSO₄, SiO₂, and polymer network—to achieve both high PLQY and commercially viable lifetime in PeNCs. This HS design

¹Department of Materials Science and Engineering, Seoul National University, Gwanak-gu, Seoul, Republic of Korea. ²Research Institute of Advanced Materials, Seoul National University, Gwanak-gu, Seoul, Republic of Korea. ³PEROLED, Gwanak-gu, Seoul, Republic of Korea. ⁴Soft Foundry, Seoul National University, Gwanak-gu, Seoul, Republic of Korea. ⁵SN Display Co., Gwanak-gu, Seoul, Republic of Korea. ⁶Department of Materials, Imperial College London, London, UK. ⁷Department of Physics, Cavendish Laboratory, University of Cambridge, Cambridge, UK. ⁸Department of Chemical Engineering and Biotechnology, University of Cambridge, Cambridge, UK. ⁹Instituto de Ciencia Molecular (ICMol), Universidad de Valencia, Catedrático José Beltrán, Paterna, Spain. ¹⁰Department of Photonics and Nanoelectronics, Hanyang University ERICA, Ansan, Republic of Korea. ¹¹HU-KITECH Joint Department, Hanyang University, Ansan, Republic of Korea. ¹²Department of Materials Science and Engineering, Korea Advanced Institute of Science and Technology (KAIST), Daejeon, Republic of Korea. ¹³Applied Science Research Institute, Korea Advanced Institute of Science and Technology (KAIST), Daejeon, Republic of Korea. ¹⁴Department of Materials Science and Engineering, University of Tennessee, Knoxville, TN, USA. ¹⁵School of Earth and Environmental Sciences, Seoul National University, Seoul, Republic of Korea. ¹⁶Institute of Applied Physics, Seoul National University, Seoul, Republic of Korea. ¹⁷Institute of Engineering Research, Interdisciplinary Program in Bioengineering, Seoul National University, Seoul, Republic of Korea. *Corresponding author. Email: twlees@snu.ac.kr, taewlees@gmail.com

introduces lattice-interface interlocking as a stabilization strategy that confines the perovskite lattice and locks the surface, which suppress degradation pathways driven by lattice softening, ion migration, and interfacial reactions. HS-MAPbBr₃ (MA, methylammonium) films exhibited 100.0% PLQY (average 98.6%), which minimized nonradiative losses and transformed self-absorption into beneficial photon recycling.

As a result, a 20 wt % film delivered an EQY of 91.4%, approaching the theoretical maximum and surpassing all reported solid emitters (EQY < 65%), including rare-earth phosphors, organics, QDs, carbon dots, metal nanoclusters, and halide perovskites. Moreover, HS-CsPbBr₃ PeNC films achieved commercially viable photoluminescence stability, with $T_{90} = 3211$ hours at accelerated 60°C, 90% RH stress and $T_{90} = 12,000$ hours under continuous 180 W/m² blue-light exposure.

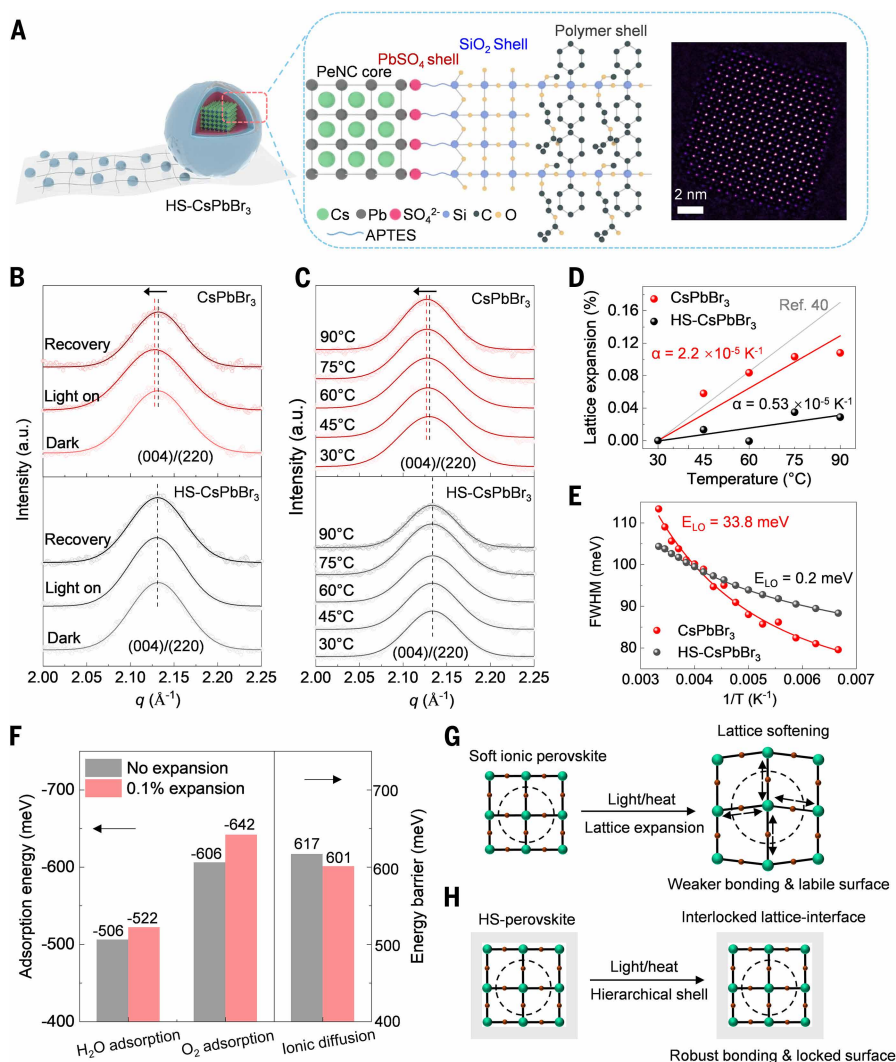


Fig. 1. HSs confined perovskite lattice. (A) Structure of hierarchical shell. (Inset) High-resolution scanning transmission electron microscopy (STEM) lattice image of a typical inner CsPbBr₃ core. (B and C) Integrated profiles (out of plane) of (top) CsPbBr₃ and (bottom) HS-CsPbBr₃ obtained from in situ (B) light irradiation and (C) heating GIWAXS experiments. (D) Expansion of lattice planes from heating experiments versus temperature, and linear fits. The gray line indicates reported thermal expansion coefficient of CsPbBr₃ PeNCs (40). (E) FWHM of PL spectra versus $1/T$ from 150 to 300 K. (F) DFT-calculated adsorption energies (E_{ads}) of H₂O and O₂ molecules and ionic migration barriers on the CsPbBr₃ surface under zero strain and 0.1% lattice expansion. A 0.1% lattice expansion was selected because photo and thermal effects were experimentally found to induce ~0.1% strain in CsPbBr₃ nanocrystals. (G and H) Scheme of lattice response to heat or light stimulation in (G) bare-PeNCs and (H) HS-PeNCs.

This HS strategy was effective across diverse compositions and enabled HS-MAPbBr₃ to achieve extended humid-thermal and photostability lifetimes, surpassing $T_{90} = 3900$ hours and estimated $T_{90} = 27,234$ hours, respectively. Last, we show that HS-PeNCs exhibited no lead leakage and excellent roll-to-roll printability and patterning compatibility, making them well suited for biocompatible, large-area, high-resolution display applications.

Synthesis of HS

The HS structure (Fig. 1A) consisted of interbonded PbSO₄, SiO₂, and siloxane polymer layers that formed a lattice-interface interlocking network. The inner PbSO₄ layer had high lattice energy (~2400 kJ/mol), directly anchored the perovskite lattice, and effectively locked surface ions and passivated surface trap states (38). The intermediate SiO₂ layer, chemically coupled by 3-triethoxysilylpropylammonium (APTES), reinforced the PbSO₄-perovskite interface. The outer siloxane polymer layer was covalently grafted to SiO₂ by Si-O bonds; this arrangement ensured uniform dispersion of PeNCs in siloxane resins and introduced additional spatial confinement and environmental shielding. This chemically interlocked multishell system simultaneously modulated lattice dynamics and surface chemistry, forming a unified stable structure that enabled efficient, stable, and solution-processable PeNCs.

HS-CsPbBr₃ PeNCs were fabricated by using a multistep process (fig. S1), enabled by the rationally designed (APTES)₂SO₄ reagent (fig. S2, A to C), which simultaneously achieved surface reconstruction and chemical anchoring. Treatment of CsPbBr₃ PeNCs with (APTES)₂SO₄ selectively etched away surface CsBr in ≤ 2 min (fig. S2, D and E) to yield a Pb²⁺-rich termination (figs. S3 and S4). Transmission electron microscopy (TEM) imaging confirmed formation of a PbSO₄ monolayer (thickness ~0.2 nm) rather than bulk deposition (figs. S1C and S4), thus avoiding lattice strain (fig. S5). This tailored PbSO₄-APTES surface passivated surface defects and boosted PLQY from 46 to 99% in CsPbBr₃ solution (fig. S2F) and also provided a chemically reactive surface to anchor the subsequent SiO₂ shells.

After PbSO₄-APTES surface reconstruction, the PeNCs were subjected to controlled hydrolysis of tetramethoxysilane (TMOS) under trace water in toluene to form a thin SiO₂ layer (thickness ~2.5 nm) (figs. S1D and S6). This thin SiO₂ layer covalently bridged to APTES; this process reinforced the perovskite-PbSO₄-SiO₂ interface while maintaining the optical and structural integrity of the PeNC cores (figs. S6 to S9). The final step involved blending CsPbBr₃-PbSO₄-SiO₂ PeNCs with siloxane precursors [diphenylsilanediol (DPSD) and methacryloxypropyltrimethoxysilane (MPTMS)], which underwent in situ polymerization to form the siloxane polymer shell (fig. S10). The polymer shell both increased dispersion stability within siloxane resins and induced cross-linked network confinement around PeNCs. This multilayered chemical interlocking delivered storage stability for >400 days without measurable PL decay (fig. S11), which is superior to those of conventional PeNC colloids

and makes HS-PeNCs ideally suited for large-scale manufacturing and long-term storage.

The uniform HS-CsPbBr₃ resin could be directly processed to form homogeneous thin films by means of bar-coating (fig. S10, F and G). During photo-curing, acrylate cross-linking within the polymer matrix further reinforced the intershell mechanical coupling and thereby formed a mechanically robust yet optically transparent network. In solid films, HS-CsPbBr₃ retained a high PLQY of 95.0% (average 92.0%) versus the PLQY of control bare-CsPbBr₃ films (32.0%; average 30.0%) (table S8). This increase reflected the critical passivation function of lattice-interface interlocked HS in suppressing solid-state nonradiative recombination (supplementary text S2). Suppressed surface trap-assisted recombination of HS-CsPbBr₃ was confirmed with transient photoluminescence (TrPL) and transient absorption (TA) analysis (figs. S12 to S14). Moreover, the HS layer weakened orbit-orbit interactions (fig. S15) and thus effectively prevented bright-to-dark state conversion and enabled high PLQY in PeNC solids.

Lattice-interface interlocking by a HS

To test whether lattice softening contributes directly to the acceleration of PeNC degradation, we conducted in situ synchrotron grazing-incidence wide-angle x-ray scattering (GIWAXS) to track lattice strain evolution under controlled conditions of illumination or thermal stress (figs. S16 to S18). Both CsPbBr₃ PeNC-siloxane film and HS-CsPbBr₃ PeNC-siloxane film showed diffraction peaks at scattering vector magnitude (q) = 1.12, 1.51, and 2.13 Å⁻¹, which were indexed to (002)/(110), (112)/(020)/(200), and (004)/(220) crystal facets, respectively (fig. S17). Among these, the (004)/(220) plane was selected for strain analysis because its high diffraction angle and multiplicative factor provided high sensitivity to changes in structural symmetry (39).

In bare-CsPbBr₃ film, blue-light illumination caused a decrease in the q of the diffraction peak of (004)/(220) (Fig. 1B, top); this change indicated photoinduced lattice expansion. This shift scaled with incident light intensity, confirming that the expansion was a direct effect of photoexcitation rather than of cumulative light dose or thermal effects (fig. S17) (40, 41). When the illumination ceased, the peak fully returned to its original position; this change demonstrated that the lattice relaxation was reversible. Light-induced lattice expansion generated tensile strain that weakened ionic bonding, leading to lattice softening. By contrast, in HS-CsPbBr₃-siloxane films, blue-light illumination had no effect on the q of the diffraction peak of (004)/(220) (Fig. 1B, bottom). This result confirmed that the HS effectively locked the perovskite lattice and thus suppressed photoinduced tensile strain.

The trends in thermal expansion upon heating from 30° to 90°C were similar to those of photo-illumination. In CsPbBr₃ films, this heating decreased the q of the diffraction peaks (Fig. 1C, top); calculations made using this shift indicated a thermal expansion coefficient $\alpha = (2.2 \pm 0.2) \times 10^{-5} \text{ K}^{-1}$, (Fig. 1D) which is near reported values for CsPbBr₃ PeNCs (40). By contrast, HS-CsPbBr₃ films showed almost no thermal expansion (Fig. 1C, bottom), with $\alpha = (0.53 \pm 0.2) \times 10^{-5} \text{ K}^{-1}$ (Fig. 1D). This comparison confirmed that the HS constrained lattice breathing and thereby anchored the ionic lattice and increased its mechanical rigidity.

This confined lattice also altered the optical response of HS-CsPbBr₃ (fig. S19). Temperature-dependent PL measurements revealed suppressed PL quenching, increased exciton-binding energy (fig. S19C), and an anomalous redshift in the PL peak (fig. S19D); the PL peak evolution shifted from anti-Varshni behavior in bare-CsPbBr₃ to Varshni behavior in HS-CsPbBr₃, providing strong evidence of lattice locking (supplementary text S3). Consistent with this lattice stabilization, the fitted longitudinal optical (LO) phonon energy reduced from 33.8 meV in bare-CsPbBr₃ to near-zero in HS-CsPbBr₃ (Fig. 1E), indicating that exciton-phonon coupling was suppressed and lattice dynamics were stabilized.

To understand how lattice expansion influences interfacial stability, we first performed density functional theory (DFT) calculations to

study molecular adsorption and ionic migration on CsPbBr₃ surfaces. A slight lattice expansion of 0.1% enhanced the adsorption of both H₂O [adsorption energy (E_{ads}) from -506 to -522 meV] and O₂ (E_{ads} from -606 to -642 meV) and lowered the migration barrier for Br ions from 617 to 601 meV (Fig. 1F and fig. S20). These results indicated that photo- or thermal-induced lattice softening not only facilitated surface hydrolysis and oxidation but also accelerated ion migration, providing theoretical support for our proposed lattice-interface interlinked degradation pathway of colloidal PeNCs. To experimentally verify these degradation pathways, we tracked the surface chemistry evolution of CsPbBr₃ films during 96 hours of aging under 60°C, 90% RH or continuous blue-light exposure using x-ray photoelectron spectroscopy (XPS). In both cases, oxidation and hydrolysis were observed, as evidenced by the emergence of Pb-O and CO₃²⁻ signals in the Pb, O, and C spectra (Fig. 2, A and B, and fig. S21). These changes directly indicated Pb-Br bond dissociation, leading to the formation of Pb(OH)₂ and PbCO₃ (27). The degradation was more pronounced under 60°C, 90% RH than under blue-light illumination, suggesting the moisture-accelerated surface reactions.

These surface-chemical changes were directly linked to structural and optical degradation of CsPbBr₃ PeNCs (supplementary text S4). Under 60°C, 90% RH (fig. S22), CsPbBr₃-siloxane film showed PL redshift and full-width at half-maximum (FWHM) broadening, which indicated defect formation and crystal fusion, whereas under blue-light exposure (fig. S23), the PL showed blueshift and FWHM narrowing, which suggested nanocrystal shrinkage due to photoinduced halide oxidation, as supported by XPS analysis. Transient PL measurements (figs. S25 and S26) showed progressive lifetime reduction and spectral evolution, which corroborated these trends. Consequently, bare-CsPbBr₃-polymer films achieved only short $T_{90} = 13$ hours under 60°C, 90% RH and 19 hours under blue-light irradiation (Fig. 2, C and D), whereas bare-CsPbBr₃-polymer films remained stable for >300 hours when stored at room temperature in dark ambient conditions. This difference emphasized that photo- and thermal-induced lattice expansion and softening strongly accelerated degradation in humid and oxygen-rich environments.

Collectively, these results provided theoretical and experimental evidence of a lattice softening-driven degradation pathway in CsPbBr₃ PeNCs, even when protected by polymer coatings. Under illumination or humid-thermal aging, photo- or thermally induced lattice expansion weakened ionic bonding, softening the ionic lattice and destabilizing the labile surface (Fig. 1G). This softening promoted surface oxidation and hydration and facilitated ion migration, ultimately triggering crystal degradation. These findings reveal that lattice softening is a critical upstream driver that initiates and accelerates both lattice and surface deterioration, giving rise to a lattice-interface interlinked degradation pathway, particularly in colloidal PeNCs with insufficient shell-to-lattice anchoring. This mechanistic insight underscores the need to simultaneously confine the lattice and stabilize the surface to achieve long-term operational stability.

By contrast, HS-CsPbBr₃ films maintained unaltered surface chemistry and structural integrity even after 3000 hours under 60°C, 90% RH and under 4000 hours under continuous blue-light exposure (Fig. 2, A and B, bottom, and fig. S27). The corresponding T_{90} reached 3211 hours under 60°C, 90% RH (Fig. 2C), whereas blue-light exposure yielded a photostability lifetime of 12,000 hours (Fig. 2D), or more than 630 times longer than that of bare-CsPbBr₃. Throughout these tests, HS-CsPbBr₃ preserved stable PL spectra with no peak shift or broadening (Fig. 2, E and F), surpassing the commercial benchmark in colloidal CsPbBr₃ films (table S7). Additional control samples with incomplete shells [CsPbBr₃-PbSO₄-siloxane, CsPbBr₃-PbSO₄-APTES-siloxane, and CsPbBr₃-PbSO₄-SiO₂-isobornyl acrylate (IBOA)] exhibiting high PLQYs (92, 93, and 88%, respectively) through PbSO₄ passivation, comparable with that of fully protected HS-CsPbBr₃, failed within tens to hundreds of hours. This difference confirmed that complete lattice-interface

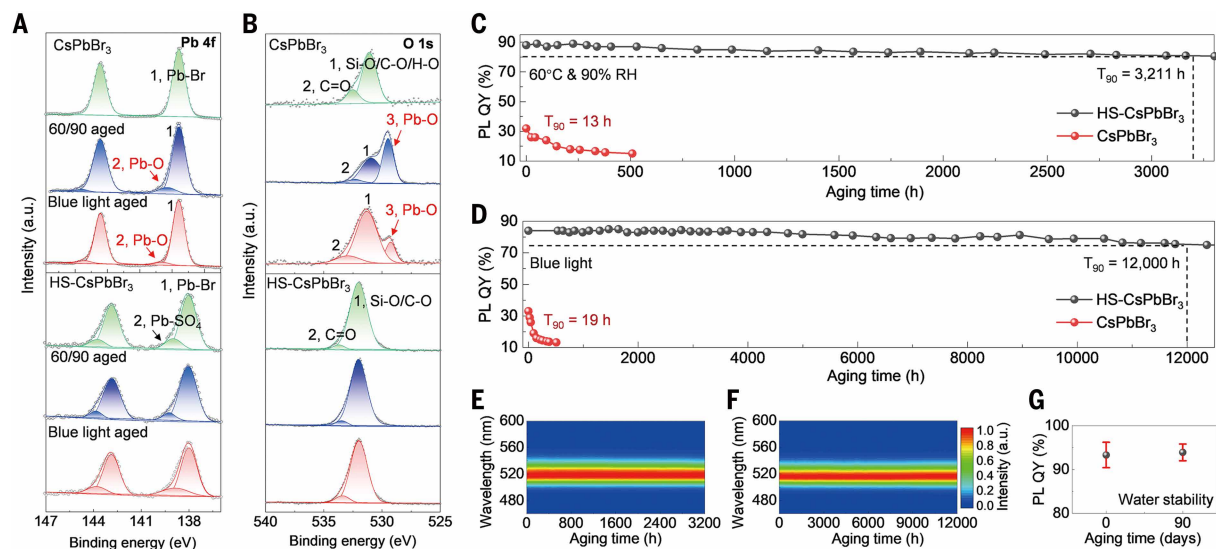


Fig. 2. Aging stability of HS-PeNCs. (A) Pb^{4f} and (B) O^{1s} XPS spectra of (top) CsPbBr₃ and (bottom) HS-CsPbBr₃ films before and after aging under 60°C, 90% RH (denoted as 60/90) and 180 W/m² blue-light irradiation. (C and D) Profiles of PLQY over aging time for CsPbBr₃ and HS-CsPbBr₃ films aging under (C) 60°C, 90% RH and (D) 180 W/m² blue light. (E and F) Profiles of PL spectra versus aging duration for HS-CsPbBr₃ films under (E) 60°C, 90% RH and (F) blue light. (G) PLQY record of HS-CsPbBr₃ in water.

interlocking by using a HS is essential for achieving long-term operational stability (supplementary text S4).

Together, these results demonstrate that the HS achieves robust lattice-interface interlocking, realized as an interbonded PbSO₄-SiO₂-polymer network that simultaneously confined the mechanically soft lattice and chemically stabilized the reactive surface (Fig. 1H). This dual protective role was crucial because it suppressed the lattice-interface interlinked degradation pathway in which lattice expansion, ion migration, and surface oxidation and hydration mutually accelerate structural and optical degradation. Furthermore, systematic variation of the Pb-salt layer [Pb(HCOO)₂, Pb₂(HPO₃)₂, PbSO₄, and Pb₃(PO₄)₂] and polymer matrix further established the design principle (supplementary text S5): Divalent Pb-salt shells [Pb₂(HPO₃)₂ or PbSO₄] were required to form interlocked interfacial layers, with PbSO₄ offering the stronger stabilization, whereas outer APTES-SiO₂-siloxane layers were indispensable for achieving full lattice-interface locking.

The robust HS protection extends beyond photoluminescence stability. HS-CsPbBr₃ maintains nearly constant PLQY after 90 days of immersion in water (Fig. 2G) and thereby demonstrates comprehensive interfacial sealing and exceptional water resistance. Furthermore, the HS barrier blocked Pb²⁺ release into water and thus ensured intrinsic environmental safety. In cytotoxicity tests that used C2C12 myoblast cells, HS-CsPbBr₃ supported healthy cell proliferation comparable with that of polystyrene culture plates and better than that of bare or partially protected PeNCs (fig. S32). Together, these findings establish that HS-PeNCs are chemically, structurally, optically, and biologically robust materials that offer long-term environmental stability for applications in displays, lighting, and bio-optoelectronic sensors.

Broad applicability of HS

Emission color of halide PeNCs can be tuned across the visible to near-infrared spectrum by adjusting their composition, APbX₃ [A = Cs, MA, or FA (formamidinium); X = Cl, Br, I, or their mixtures]. However, ensuring long-term optical stability across this compositional space is highly challenging owing to photoinduced halide-phase separation in mixed-halide and -cation systems, oxidation susceptibility in iodide-rich compositions, and structural fragility of organic-inorganic hybrids. These composition-dependent degradation pathways have so far precluded the development of a universal strategy that simultaneously

increases stability and luminescent efficiency across diverse PeNC compositions.

We systematically applied the lattice-interface interlocking HS strategy to representative lead halide PeNC compositions from all inorganic, organic-inorganic hybrid, mixed-halide, pure-iodide, and mixed-cation systems. The HS successfully stabilized all of these compositions to produce composition-tunable PeNC resins and films with precisely tunable emission wavelengths from 409 to 783 nm (Fig. 3, A to C, and fig. S33). All HS-PeNC resins formed uniform and aggregation-free solid films (Fig. 3, C to F). In both solution and solid states, the HS consistently passivated surface defects and increased the PLQY in all compositions (Fig. 3G and table S10), with pure-bromide and iodide-rich systems achieving near-unity PLQY. These outstanding emissive properties arose from the broad lattice compatibility of the HS structure, which accommodated different halide perovskite compositions without introducing substantial interfacial strain (supplementary text S6).

The HS also consistently extended both humid-thermal and photostability lifetimes, with photostability of all tested compositions increasing by more than two orders of magnitude from several tens of hours to well over 1000 hours (Fig. 3, H and I; figs. S35 to S37; and table S11). In particular, red-emitting CsPbBr_{1.2}I_{1.8} PeNCs, which typically underwent rapid photoinduced phase separation, had only 11 hours of photostability in bare-CsPbBr_{1.2}I_{1.8} films, whereas HS-CsPbBr_{1.2}I_{1.8} retained stable emission and composition for >2000 hours under continuous blue-light exposure (180 W/m²). This increase emphasized the effectiveness of HS-mediated lattice anchoring (fig. S35). Similarly, iodide-rich APbI₃ (A = Cs, FA, or CsFA)PeNCs had poor phase stability and high susceptibility to photo- and thermo-oxidation and therefore degraded within ~10 hours under humid-thermal and light-aging conditions, but the HS protection increased their humid-thermal lifetimes by >10 times and their photostability lifetimes by >100 times.

Hybrid perovskites such as MAPbBr₃ are valued for their ITU-R Recommendation BT.2020 (Rec. 2020)-compatible pure-green emission but have a softer lattice than that of inorganic perovskite, and this trait presents additional stabilization challenges. Nevertheless, the HS structure effectively provided lattice-interface interlocking (figs. S38 and S39) and achieved 100.0% PLQY (average: 98.6%). HS-MAPbBr₃ films exhibited an extended T₉₀ of 3900 hours under 60°C,

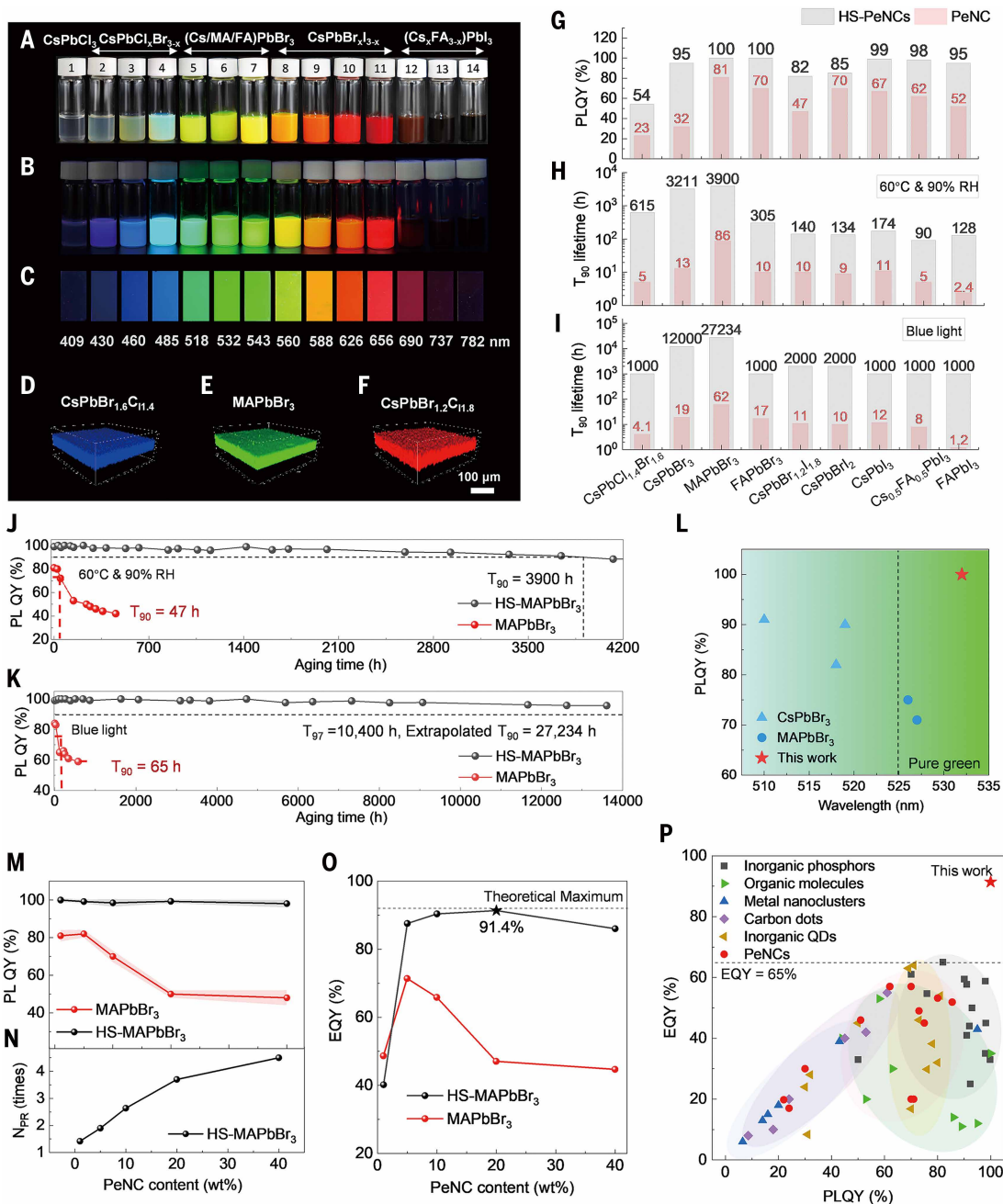


Fig. 3. Broad applicability of hierarchical shells. (A to C) Optical image of composition-tunable HS-PeNCs in siloxane resins under (A) daylight and (B) UV light and (C) in films under UV light. (D to F) PL confocal microscope image of (D) blue, (E) green, and (F) red HS-PeNC films. (G) PLQY, (H) T_{90} under 60°C, 90% RH, and (I) T_{90} under 180 W/m² blue light of nine typical compositions of bare-PeNCs and HS-PeNCs. (J and K) Profiles of PLQY versus aging duration for MAPbBr₃ and HS-MAPbBr₃ films under (J) 60°C, 90% RH and (K) blue light. In (K), the T_{90} lifetime is estimated by means of stretched-exponential fit extrapolation (fig. S40). (L) PLQY versus emission peak for reported colloidal PeNC solid emitters that exhibited high stability under both the 60°C, 90% RH and blue-light exposure conditions, based on data from table S7. (M) PLQY profiles with increased HS-MAPbBr₃ concentrations in 50- μ m film, excited at 450 nm. (N) Number of photo-recycling times of HS-MAPbBr₃ versus PeNC concentration. (O) EQY profiles versus PeNC concentration. (P) EQY versus PLQY for various light emitters excited at 365 to 450 nm, based on data from tables S1 to S6.

90% RH (3.9 times the 1000-hours commercial benchmark) and an extrapolated T_{90} of 27,234 hours (~37 months) under continuous blue light, which is 2.7 times the 10,000-hours benchmark (Fig. 3, J and K; fig. S40; and table S12); these were both immense improvements over control bare-MAPbBr₃-siloxane films, which degraded within 86 hours under humid-thermal stress and 62 hours under continuous blue light. We also demonstrated stable near-unity PLQY in pure-green colloidal PeNC films

(525 to 535 nm) (Fig. 3L and table S7) and surpassed even commercial CdSe-ZnS-polymer QDs in both efficiency and stability (fig. S41).

Moreover, the HS process achieved outstanding batch-to-batch reproducibility, with 10 consecutive batches of HS-MAPbBr₃ films consistently exceeding commercial aging benchmarks (fig. S42). Collectively, these results established the HS as a universal, compositionally adaptable, and highly reproducible stabilization method that

offered robust protection and improved efficiency for lead halide PeNCs of all compositions and emission colors.

Near-unity QY eliminates self-absorption loss

Lead halide PeNCs, including MAPbBr₃, exhibited direct band-to-band transitions, large absorption coefficients, and small Stokes shifts (42), which exacerbated self-absorption losses at high concentrations (17). In the bare-MAPbBr₃ films, we observed a concentration-dependent PLQY decay from 81% at 1 wt % to 48% at 40 wt % (Fig. 3M), highlighting the severity of this issue. By contrast, HS-MAPbBr₃ films with 100% PLQY resulted in near-complete suppression of nonradiative recombination and enabling efficient photon recycling. As concentration increased from 1 to 40 wt %, absorptance rose accordingly, accompanied by slight redshifts in PL spectra and prolonged PL lifetimes—signatures of enhanced photon recycling (figs. S43 and S44).

Quantitative modeling (supplementary text S7) revealed that the average number of photon recycling events (N_{PR}) increased from 1.42 at 1 wt % to 4.49 at 40 wt % (Fig. 3N), whereas the corresponding photon recycling efficiency (η_{PR}) increased from 0.267 to 0.777 (table S13). These effects were fundamentally enabled by the near-unity PLQY, which ensured that nearly all reabsorbed photons were reemitted rather than lost to nonradiative decay. Thus, self-absorption was transformed from a loss mechanism into a photon reuse pathway, allowing light to be recycled multiple times before escaping the film. Additionally, HS-MAPbBr₃ PeNCs enhanced light scattering within the siloxane film (supplementary text S8), mitigating optical losses from waveguided modes and improving light outcoupling. As a result, PLQY remained exceptionally high across the entire concentration range, decreasing only slightly from 100.0% at 1 wt % to 98.1% at 40 wt % (Fig. 3M and fig. S45), with corresponding internal PLQY consistently above 99.6% (table S13). This quenching-resistant process validated the reliability of near-unity PLQY in HS-MAPbBr₃ films (fig. S46).

Accordingly, the 20 wt % HS-MAPbBr₃ film achieved an EQY of 91.4% (Fig. 3O), approaching the theoretical maximum of 92.0% for MAPbBr₃-siloxane composites (supplementary text S9) and surpassing all previously reported solid emitters, including rare-earth and transition metal phosphors, organic emitters, QDs, carbon dots, metal nanoclusters, and other halide perovskites excited in the range of commercial light sources (365 to 450 nm) (Fig. 3P and tables S1 to S6). This quenching resistance also translated to exceptional device performance, achieving a record color-conversion efficiency of 69.6% versus a previously reported value of 52%, with near-zero blue leakage when applied onto blue light-emitting diodes (LEDs) (figs. S49 and S50 and supplementary text S10). Together, these results established HS-PeNCs as a new class of quenching-resistant, high-efficiency, and stable emitters, ideal for next-generation color-conversion displays, solid-state lighting, solar concentrators, and scintillators.

Processability and applications of HS-PeNCs

Colloidal PeNCs have excellent solution processability, but during solid-state deposition, their unstable surface ligands often lead to defects and aggregation, which degrade optical characteristics and limit the scalability of fabrication. By contrast, HS-PeNCs, stably dispersed in siloxane resins, displayed high processability and long-term colloidal stability, which facilitated high-quality film formation across various processing platforms. Large-area uniform green and red PeNC-polymer films were fabricated by using roll-to-roll printing (Fig. 4A and fig. S51). Uniform PeNC patterning was achieved with inkjet printing (fig. S52). Micropatterns down to 3 μm [pixel density of 3522 pixels per inch (PPI)], which meets the required resolution of micro-LED displays for augmented reality (AR) and virtual reality (VR) applications, can be achieved with high-resolution photolithography (Fig. 4B and fig. S53).

Compared with previously reported stabilization strategies on colloidal PeNCs, the HS offers a comprehensive improvement in five

essential attributes: PLQY, stability, compositional adaptability (universality), cytotoxicity, and processability (Fig. 4C and table S7). To demonstrate industrial scalability, we fabricated 4K prototype display panels (3840 by 2160 pixels) by incorporating green HS-MAPbBr₃ PeNCs into color-conversion films (Fig. 4, D to F). The incorporation of HS-MAPbBr₃ PeNCs broadened the display's color gamut coverage (Fig. 4D) and enhanced imaging quality (Fig. 4E). By exploiting the excellent compatibility of HS-PeNCs with standard display processing, we fabricated prototype 10.1-inch tablets, 28- and 32-inch monitors, and 43- and 75-inch televisions, all demonstrating uniform brightness and vivid color rendering (Fig. 4F and supplementary movies S1 to S5). These displays achieved color-gamut area ratios >97% of Rec. 2020, 131% of NTSC (National Television Standards Committee), and 185% of sRGB (standard red green blue) (table S16), which exceeded those of commercialized liquid crystal displays (LCDs), InP QDs, and organic LED (OLED) tablets and monitors (figs. S54 and S55). This exceptional color gamut coverage originated from the narrowband and highly efficient pure-green emission of HS-MAPbBr₃.

Besides the display applications, flexible HS-PeNC films also show strong potential as light sources for wearable biomedical sensors, owing to combined high lead retention; structural robustness; and composition-tunable, narrowband red-to-near-infrared (NIR) emission. These attributes make HS-PeNCs particularly suitable for photoplethysmography or other bio-optoelectronic applications (fig. S56 and supplementary text S11).

Conclusions

We developed a lattice-interface interlocking stabilization strategy that uses a HS architecture with interbonded PbSO₄-SiO₂-polymer layers to achieve both high PLQY and commercially viable lifetime in colloidal PeNC solids. This approach minimizes the root cause of PeNC instability, a lattice-interface interlinked degradation pathway, in which lattice softening and surface reaction cooperatively accelerate structural and optical deterioration. Mechanistically, the lattice-interface interlocking HS simultaneously locks the soft lattice and stabilizes the surface, suppressing light- or heat-induced expansion and surface reaction, preserving optical performance under stress. As a result, HS-MAPbBr₃ films retain 100.0% PLQY (average 98.6%) and exhibit exceptional stability, with T_{90} = 3900 hours at 60°C, 90% RH and 27,234 hours under continuous blue-light exposure, surpassing commercial benchmarks.

Such high PLQY transforms self-absorption into beneficial photon recycling and thus overcomes the absorptance-PLQY trade-off in various solid emitters, delivering an EQY of 91.4%, which is close to the theoretical maximum. HS-PeNCs exhibit no lead leakage and are compatible with roll-to-roll printing and high-resolution patterning, which makes them viable for scalable, high-resolution display technologies. Moreover, the HS strategy generalizes across diverse PeNC compositions, including mixed-halide, mixed-cation, iodide, and organic-inorganic hybrid systems and enabling long-lifetime, color-stable emission across the visible-to-NIR spectrum. More broadly, this lattice-interface interlocking concept offers a transferable design principle for stabilizing soft halide perovskite materials and optoelectronics, which has long been hampered by insufficient operational lifetime.

Materials and methods

Chemicals

3-Aminopropyltriethoxysilane (APTES, 99%), sulfuric acid (99.999%), cesium carbonate (Cs₂CO₃, 99.9%), oleic acid (OA, technical grade 90%), oleylamine (OAm, technical grade 70%), 1-octadecene (ODE, technical grade 90%), PbBr₂ (98%), PbCl₂ (99%), toluene (anhydrous), methyl acetate (MeOAc, anhydrous), *N,N*-dimethylformamide (DMF, 99.8%), isopropanol (IPA, anhydrous), tetramethoxysilane (TMOS, 99%), barium hydroxide monohydrate, 2,2-dimethoxy-2-phenylacetophenone (BDK), phenylbis(2,4,6-trimethylbenzoyl)phosphine oxide

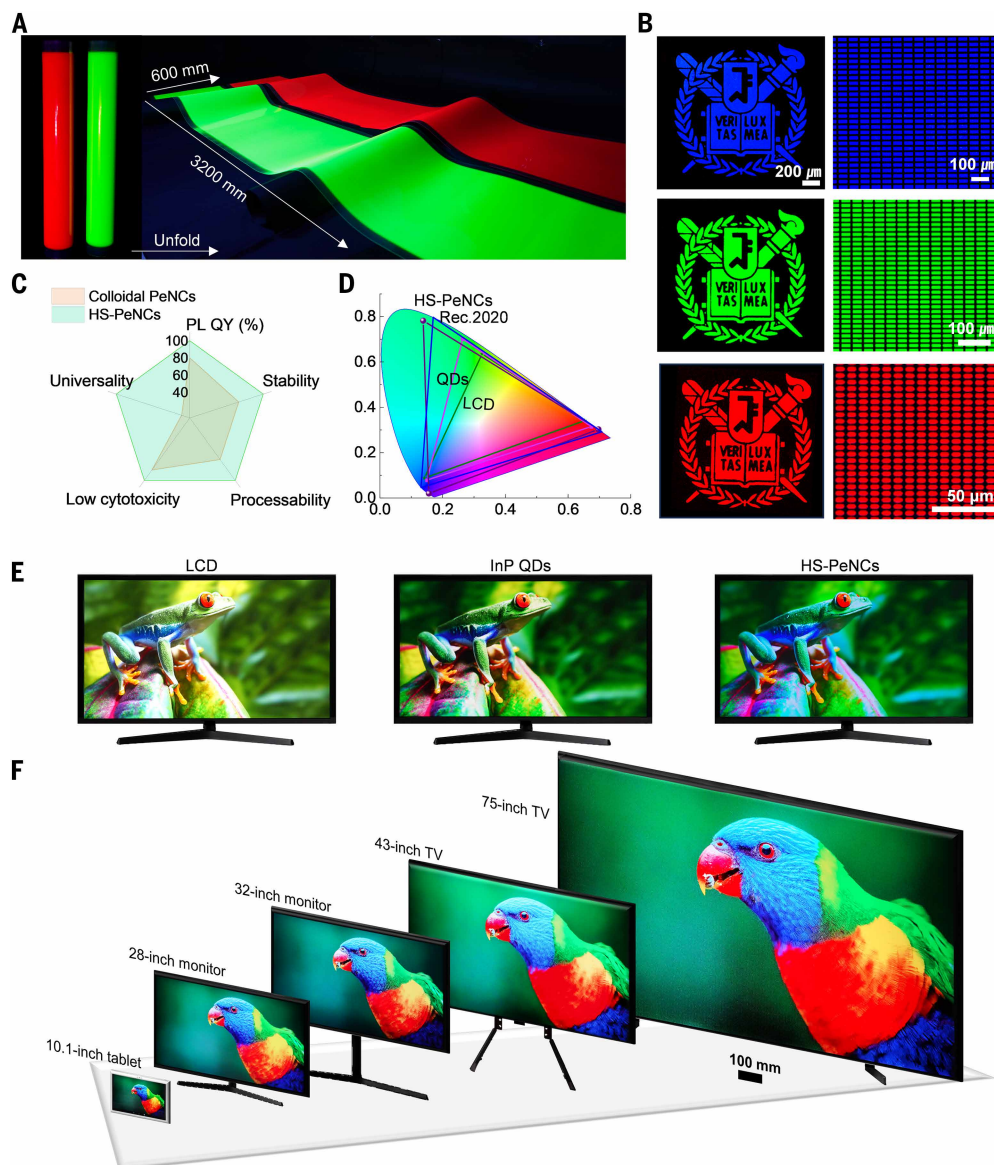


Fig. 4. Processability and display applications of HS-PeNCs. (A) Optical images (under UV light) of large-area flexible green HS-MAPbBr₃ and red HS-CsPbBr_{1.21.8} PeNC films obtained by means of roll-to-roll printing. (B) The Seoul National University emblem and rectangular micropatterns with varying sizes fabricated by means of photolithography on HS-PeNC films. Rectangular pixels and their corresponding resolutions are 50 by 20 μm (405 PPI), 30 by 10 μm (667 PPI), and 6 by 3 μm (3522 PPI) for blue, green, and red micropatterns, respectively. (C) Comparison of performance criteria of HS-PeNCs with other reported fabrication methods in colloidal PeNCs (table S7). (D) Color gamut coverage of HS-PeNCs compared with commercialized LCD and InP QDs. (E) Photographs of 28-inch display panels incorporating LCD, InP QDs, and HS-PeNCs. (F) Prototype demonstrations of various-size displays that used HS-PeNCs. On-screen images are used for illustrative purposes only. [Credit: Frog images and parrot, iStock.com/ABDESIGN and iStock.com/tracioulouse (used under license).]

(Irgacure 819), diphenyl(2,4,6-trimethylbenzoyl)phosphine oxide (TPO), formic acid (HCOOH, 98%), triethylphosphine (TOP), phosphoric acid (H₃PO₄, 99.99%), chloroform (99.8%), acetonitrile (99.5%), and phosphorous acid (H₃PO₃, 99%) were purchased from Sigma-Aldrich. Lead(II) iodide (PbI₂, 99.9985%) and *n*-decylamine were purchased from Alfa Aesar. FABr, MABr, and FAI were purchased from Dyesol. Diphenylsilanediol (DPDS), 3-methacryloxypropyltrimethoxysilane (MPTMS), and 2-isopropylthioxanthone (ITX) were purchased from TCI. 1-Butanol was purchased from Samchun. Polymer-ligand-capped CdSe/ZnS QDs were purchased from Dong-A Carbon Tech. All chemicals were used without further purification.

Synthesis of (APTES)₂SO₄ and its solutions

(APTES)₂SO₄ was prepared by reacting 0.8 mmol APTES with 0.4 mmol of H₂SO₄ in anhydrous IPA. The (APTES)₂SO₄ solid was obtained by drying the reaction mixture in a vacuum oven and used for further characterization. To prepare (APTES)₂SO₄ solution for growing core-shell PeNCs, 0.4 mmol of (APTES)₂SO₄ was dispersed in a mixed solvent composed of 9.5 ml of toluene, 0.5 ml of anhydrous isopropanol, and 0.2 ml of oleic acid (pre-dried at 120°C for 1 hour under reduced pressure).

The APTES-HCOO, (APTES)₂HPO₃, and (APTES)₃PO₄ complexes were synthesized following the same procedure as (APTES)₂SO₄, except that H₂SO₄ was replaced with HCOOH, H₃PO₃, and H₃PO₄, respectively.

Synthesis of CsPbBr₃ PeNC cores

50 ml of ODE, 5 ml of oleic acid and 5 ml of oleylamine and 800 mg of PbBr₂ were loaded into a 250-ml three-necked flask, degassed and dried at 120°C for 1 hour under vacuum (24). Then the temperature was elevated to 210°C, and 8 ml of Cs-oleate precursor (0.125 M in ODE) was quickly injected under N₂ atmosphere. After 10 s, the solution was quenched in an ice-water bath, then the CsPbBr₃ PeNCs were precipitated by adding MeOAc at an ODE:MeOAc volume ratio of 1:2 and centrifuged at 7,200 rpm for 3 min. The precipitate was redispersed in 18 ml of toluene, precipitated by adding 18 ml of MeOAc, and centrifuged again at 7,200 rpm for 3 min. Finally, CsPbBr₃ PeNCs were dispersed in toluene to coat them with a hierarchical shell. All purification steps were performed in air.

Synthesis of CsPbBr₃-PbSO₄·SiO₂ double-shell PeNCs

First, 218 mg of CsPbBr₃ were dispersed into a 100 ml vial and dispersed in 87.2 ml of anhydrous toluene to form a solution with a concentration of 2.5 mg/ml. Then 4.41 ml of (APTES)₂SO₄ solution was added, and the mixture was stirred for 12 hours. To grow the SiO₂ shell, 105 μl of TMOS was added in three steps: first, 17.5 μl of TMOS, then 35 μl of TMOS after 1 hour, and then 51.5 μl of TMOS after another 1 hour. The vial was heated at 30°C on a hot plate and exposed to air (50 to 75% relative humidity) to facilitate hydrolysis of TMOS and formation of the SiO₂ shell.

Preparation of HS-CsPbBr₃ siloxane resins and films

HS-CsPbBr₃ siloxane resins were formed by an in situ sol-gel reaction of MPTMS and DPDS (1:1 molar ratio) in the presence of CsPbBr₃-PbSO₄·SiO₂ double-shell PeNCs. In this process, the hydroxyl groups

(–Si–OH) in DPSD enable the sol–gel reactions (condensation reactions between the hydroxyl group of DPSD and the methoxy group of MPTMS to form Si–O–Si bonds) without additional water (32). Barium hydroxide monohydrate was added as a base catalyst to promote the sol–gel reaction. The mixture of PeNCs and silane precursors were held at 80°C under vacuum for 8 hours. Photo-initiators (2 wt%) were added to the HS-CsPbBr₃ siloxane resin prior to UV curing. Films were prepared by bar-coating onto PET and UV-curing at 100 mW/cm² for 3 min. Unless otherwise noted, characterizations and aging tests were performed on 100-μm-thick films.

The HS-CsPbBr₃ siloxane resins and films employing Pb(HCOO)₂, Pb₂(HPO₃)₂, and Pb₃(PO₄)₂ shells were prepared identically, substituting APTES-HCOO, (APTES)₂HPO₃, or (APTES)₃PO₄ for (APTES)₂SO₄, respectively.

Yield of HS-PeNCs

The multistep HS synthesis maintained high material yield. During PbSO₄/SiO₂ deposition, no detectable degradation of PeNCs was observed, and the resulting double-shelled CsPbBr₃/PbSO₄/SiO₂ nanocrystals were fully recovered by centrifugation, with yields approaching 100%. In the subsequent in situ polymerization using DPSD and MPTMS, material loss (~25%) was attributed to precursor adhesion to the reaction vessel. For example, starting from 13.3 g of precursors (7.1 g MPTMS and 6.2 g DPSD), ~10 g of HS-PeNC-siloxane composite was obtained, corresponding to an overall synthetic yield of ~75%.

Synthesis of CsPbX₃ (X = Cl, Br, I, or their mixtures) PeNCs

CsPbX₃ PeNCs were synthesized following the synthetic route toward CsPbBr₃ PeNCs, except that the precursors were changed as follows: CsPbCl₃ (606 mg PbCl₂, 5 ml TOP); CsPbCl₂Br (444 mg PbCl₂, 213 mg PbBr₂); CsPbCl_{1.4}Br_{1.6} (293 mg PbCl₂, 413 mg of PbBr₂); CsPbClBr₂ (182 mg PbCl₂, 560 mg PbBr₂); CsPbBr₂I (533 mg PbBr₂, 333 mg PbI₂); CsPbBr_{1.7}I_{1.3} (453 mg PbBr₂, 433 mg PbI₂); CsPbBr_{1.2}I_{1.8} (320 mg PbBr₂, 600 mg PbI₂); CsPbBrI₂ (266 mg PbBr₂, 668 mg PbI₂); CsPbI₃ PeNCs (1,000 mg PbI₂). The purification procedure for CsPbX₃ PeNCs was the same as for CsPbBr₃ PeNCs.

Synthesis of MAPbBr₃ and FAPbBr₃ PeNCs

MAPbBr₃ PeNCs were synthesized in air at room temperature based on the reported protocol (43). MAPbBr₃ precursor solutions were prepared by dissolving 0.2 mmol of MABr and 0.1 mmol of PbBr₂ in 0.5 ml of DMF. Then 0.15 ml of precursor solution was injected into a crystallization-inducing solution that was composed of 0.02 ml of *n*-decylamine, 0.3 ml of oleic acid, 2 ml of 1-butanol and 5 ml of toluene. The reaction was complete after 10 min of vigorous stirring. The resulting colloidal PeNCs were collected by sequential centrifugation at 12,000 rpm for 10 min, and then dispersed in toluene. The reaction could be scaled up to 600 times for mass production (total volume was ~4440 ml).

FAPbBr₃ PeNCs were prepared using the same procedure, except that FABr replaced the MABr precursor.

Synthesis of FAPbI₃ PeNCs

FAPbI₃ PeNCs were synthesized in air at room temperature. FAPbI₃ precursor solutions were prepared by dissolving 0.1 mmol of FAI, 0.05 mmol of PbI₂, 0.6 ml of oleic acid, and 100 μl of oleylamine in 0.5 ml of DMF. Then 0.3 ml of precursor solution was injected into 10 ml of chloroform solution, and reaction was complete after 1 min of vigorous stirring. The colloidal PeNCs with desired size were collected by adding 0.5 ml of acetonitrile and sequential centrifugation at 7200 rpm for 3 min and then dispersed in toluene.

Synthesis of Cs_{0.5}FA_{0.5}PbI₃ PeNCs

Cs_{0.5}FA_{0.5}PbI₃ PeNCs were synthesized using cation-exchange: 17 mg of FAPbI₃ and 21.6 mg of CsPbI₃ were mixed in a toluene solution that contained 5 μl of OA and 3 μl of OAm. The reaction was complete after

stirring for 30 min. MeOAc (twice the total volume of the PeNCs suspension) was added to precipitate the PeNCs. The powders were dispersed in toluene, then centrifuged at 4000 rpm for 5 min to collect the supernatant.

Synthesis of color- and composition-tunable HS-APbX₃ (A = Cs, MA or FA; X = Cl, Br, I or their mixtures) siloxane resins and films

Color- and composition-tunable HS-APbX₃ resins and films were prepared using the same procedure that was used to synthesize HS-CsPbBr₃ resin and film, except that different PeNCs were used.

Monitoring aging stability of HS-PeNC films

Films were aged in a humid-thermal chamber (60°C, 90% RH), immersed in water, or irradiated with blue light (180 W/m²). For blue-light aging, films were positioned 1 cm from the LEDs. Samples were periodically removed for PLQY and spectral measurements using a JASCO FP-8500 spectrofluorometer. No additional encapsulation was used during aging.

Summary of supplementary materials

Additional experimental details are provided in the supplementary materials, including synthesis of PeNC cores and HSs, preparation of siloxane composites and films, and device fabrication and characterization methods. Extended structural, optical, and stability analyses are provided in figs. S1 to S56 and tables S1 to S16, along with benchmarking of solid-state emitters. Supplementary text S1 to S11 offer further mechanistic discussion and theoretical modeling. References (43–116) list additional literature cited. Supplementary movies S1 to S5 show demonstrations enabled by HS-PeNC films.

REFERENCES AND NOTES

- H. W. Leverenz, Luminescent solids (phosphors). *Science* **109**, 183–195 (1949). doi: [10.1126/science.109.2826.183](https://doi.org/10.1126/science.109.2826.183); pmid: [17800950](https://pubmed.ncbi.nlm.nih.gov/17800950/)
- S. Liu *et al.*, Direct observation of circularly polarized nonlinear optical activities in chiral hybrid lead halides. *J. Am. Chem. Soc.* **146**, 11835–11844 (2024). doi: [10.1021/jacs.4c00619](https://doi.org/10.1021/jacs.4c00619); pmid: [38570347](https://pubmed.ncbi.nlm.nih.gov/38570347/)
- L. Wang *et al.*, Efficient perovskite LEDs with tailored atomic layer number emission at fixed wavelengths. *Sci. Adv.* **11**, eadp9595 (2025). doi: [10.1126/sciadv.adp9595](https://doi.org/10.1126/sciadv.adp9595); pmid: [39951530](https://pubmed.ncbi.nlm.nih.gov/39951530/)
- Y. Gao *et al.*, Highly efficient blue light-emitting diodes based on mixed-halide perovskites with reduced chlorine defects. *Sci. Adv.* **10**, eado5645 (2024). doi: [10.1126/sciadv.ado5645](https://doi.org/10.1126/sciadv.ado5645); pmid: [39018409](https://pubmed.ncbi.nlm.nih.gov/39018409/)
- X. Lin *et al.*, Electrically-driven single-photon sources based on colloidal quantum dots with near-optimal antibunching at room temperature. *Nat. Commun.* **8**, 1132 (2017). doi: [10.1038/s41467-017-01379-6](https://doi.org/10.1038/s41467-017-01379-6); pmid: [29070867](https://pubmed.ncbi.nlm.nih.gov/29070867/)
- X. Sun *et al.*, Diffusion-mediated synthesis of high-quality organic–inorganic hybrid perovskite nanocrystals. *Nat. Synth.* **4**, 167 (2024). doi: [10.1038/s44160-024-00678-3](https://doi.org/10.1038/s44160-024-00678-3)
- C. Zhu *et al.*, Supramolecular assembly of blue and green halide perovskites with near-unity photoluminescence. *Science* **383**, 86–93 (2024). doi: [10.1126/science.adi4196](https://doi.org/10.1126/science.adi4196); pmid: [38175897](https://pubmed.ncbi.nlm.nih.gov/38175897/)
- H. Zhu *et al.*, Highly efficient non-rare-earth red emitting phosphor for warm white light-emitting diodes. *Nat. Commun.* **5**, 4312 (2014). doi: [10.1038/ncomms5312](https://doi.org/10.1038/ncomms5312); pmid: [25002064](https://pubmed.ncbi.nlm.nih.gov/25002064/)
- Y. Khan *et al.*, Synthesis of fluorescent organic nano-dots and their application as efficient color conversion layers. *Nat. Commun.* **13**, 1801 (2022). doi: [10.1038/s41467-022-29403-4](https://doi.org/10.1038/s41467-022-29403-4); pmid: [35379797](https://pubmed.ncbi.nlm.nih.gov/35379797/)
- S. Zhu *et al.*, Highly photoluminescent carbon dots for multicolor patterning, sensors, and bioimaging. *Angew. Chem. Int. Ed.* **52**, 3953–3957 (2013). doi: [10.1002/anie.201300519](https://doi.org/10.1002/anie.201300519); pmid: [23450679](https://pubmed.ncbi.nlm.nih.gov/23450679/)
- Z. Han *et al.*, Ultrastable atomically precise chiral silver clusters with more than 95% quantum efficiency. *Sci. Adv.* **6**, eaay0107 (2020). doi: [10.1126/sciadv.aay0107](https://doi.org/10.1126/sciadv.aay0107); pmid: [32083176](https://pubmed.ncbi.nlm.nih.gov/32083176/)
- D. A. Hanifi *et al.*, Redefining near-unity luminescence in quantum dots with photothermal threshold quantum yield. *Science* **363**, 1199–1202 (2019). doi: [10.1126/science.aat3803](https://doi.org/10.1126/science.aat3803); pmid: [30872520](https://pubmed.ncbi.nlm.nih.gov/30872520/)
- T. J. Milstein, D. M. Kroupa, D. R. Gamelin, Picosecond quantum cutting generates photoluminescence quantum yields over 100% in ytterbium-doped CsPbCl₃ nanocrystals. *Nano Lett.* **18**, 3792–3799 (2018). doi: [10.1021/acs.nanolett.8b01066](https://doi.org/10.1021/acs.nanolett.8b01066); pmid: [29746137](https://pubmed.ncbi.nlm.nih.gov/29746137/)
- D. Zhou *et al.*, Impact of host composition, codoping, or tridoping on quantum-cutting emission of ytterbium in halide perovskite quantum dots and solar cell applications. *Nano Lett.* **19**, 6904–6913 (2019). doi: [10.1021/acs.nanolett.9b02139](https://doi.org/10.1021/acs.nanolett.9b02139); pmid: [31503498](https://pubmed.ncbi.nlm.nih.gov/31503498/)

15. T. Gong *et al.*, Quantum dot luminescence microspheres enable ultra-efficient and bright micro-LEDs. *Adv. Mater.* **37**, e2411999 (2025). doi: [10.1002/adma.202411999](https://doi.org/10.1002/adma.202411999); pmid: [39838738](https://pubmed.ncbi.nlm.nih.gov/39838738/)
16. C. Kang *et al.*, Quantum-rod on-chip LEDs for display backlights with efficacy of 149 lm W⁻¹: A step toward 200 lm W⁻¹. *Adv. Mater.* **33**, e2104685 (2021). doi: [10.1002/adma.202104685](https://doi.org/10.1002/adma.202104685); pmid: [34632633](https://pubmed.ncbi.nlm.nih.gov/34632633/)
17. J. Lin *et al.*, Perovskite quantum dots glasses based backlit displays. *ACS Energy Lett.* **6**, 519–528 (2021). doi: [10.1021/acseenergylett.0c02561](https://doi.org/10.1021/acseenergylett.0c02561)
18. International Energy Agency (IEA), “World energy outlook” (IEA, 2023).
19. IEA, “Energy efficiency” (IEA, 2022).
20. United Nations Environment Programme (UNEP), “U4E lighting report” (UNEP, 2023).
21. Natural Resources Defense Council (NRDC), “Slashing energy use in televisions” (NRDC, 2019).
22. Y.-H. Kim *et al.*, Comprehensive defect suppression in perovskite nanocrystals for high-efficiency light-emitting diodes. *Nat. Photonics* **15**, 148–155 (2021). doi: [10.1038/s41566-020-00732-4](https://doi.org/10.1038/s41566-020-00732-4)
23. H. Utzat *et al.*, Coherent single-photon emission from colloidal lead halide perovskite quantum dots. *Science* **363**, 1068–1072 (2019). doi: [10.1126/science.aau7392](https://doi.org/10.1126/science.aau7392); pmid: [30792359](https://pubmed.ncbi.nlm.nih.gov/30792359/)
24. L. Protesescu *et al.*, Nanocrystals of cesium lead halide perovskites (CsPbX₃, X = Cl, Br, and I): Novel optoelectronic materials showing bright emission with wide color gamut. *Nano Lett.* **15**, 3692–3696 (2015). doi: [10.1021/nl5048779](https://doi.org/10.1021/nl5048779); pmid: [25633588](https://pubmed.ncbi.nlm.nih.gov/25633588/)
25. T.-W. Lee, Y.-H. Kim, H.-C. Cho, “Wavelength conversion substance, manufacturing method of the same and light-emitting device comprising the same,” patent application no. KR20160054735 (Republic of Korea, 2014).
26. D. H. Kim *et al.*, Surface-binding molecular multipods strengthen the halide perovskite lattice and boost luminescence. *Nat. Commun.* **15**, 6245 (2024). doi: [10.1038/s41467-024-49751-7](https://doi.org/10.1038/s41467-024-49751-7); pmid: [39048540](https://pubmed.ncbi.nlm.nih.gov/39048540/)
27. S. Huang *et al.*, Morphology evolution and degradation of CsPbBr₃ nanocrystals under blue light-emitting diode illumination. *ACS Appl. Mater. Interfaces* **9**, 7249–7258 (2017). doi: [10.1021/acsmi.6b14423](https://doi.org/10.1021/acsmi.6b14423); pmid: [28181794](https://pubmed.ncbi.nlm.nih.gov/28181794/)
28. Y. Shen *et al.*, Strain regulation retards natural operation decay of perovskite solar cells. *Nature* **635**, 882–889 (2024). doi: [10.1038/s41586-024-08161-x](https://doi.org/10.1038/s41586-024-08161-x); pmid: [39401517](https://pubmed.ncbi.nlm.nih.gov/39401517/)
29. L. A. Muscarella *et al.*, Lattice compression increases the activation barrier for phase segregation in mixed-halide perovskites. *ACS Energy Lett.* **5**, 3152–3158 (2020). doi: [10.1021/acseenergylett.0c01474](https://doi.org/10.1021/acseenergylett.0c01474); pmid: [33072865](https://pubmed.ncbi.nlm.nih.gov/33072865/)
30. Q. Li *et al.*, Graphene-polymer reinforcement of perovskite lattices for durable solar cells. *Science* **387**, 1069–1077 (2025). doi: [10.1126/science.adu5563](https://doi.org/10.1126/science.adu5563); pmid: [40048541](https://pubmed.ncbi.nlm.nih.gov/40048541/)
31. J. De Roo *et al.*, Highly dynamic ligand binding and light absorption coefficient of cesium lead bromide perovskite nanocrystals. *ACS Nano* **10**, 2071–2081 (2016). doi: [10.1021/acsnano.5b06295](https://doi.org/10.1021/acsnano.5b06295); pmid: [26786064](https://pubmed.ncbi.nlm.nih.gov/26786064/)
32. J. Jang *et al.*, Extremely stable luminescent crosslinked perovskite nanoparticles under harsh environments over 1.5 years. *Adv. Mater.* **33**, e2005255 (2021). doi: [10.1002/adma.202005255](https://doi.org/10.1002/adma.202005255); pmid: [33617075](https://pubmed.ncbi.nlm.nih.gov/33617075/)
33. Q. Pan *et al.*, Ultrahigh stability of perovskite nanocrystals by using semiconducting molecular species for displays. *ACS Nano* **16**, 12253–12261 (2022). doi: [10.1021/acsnano.2c03062](https://doi.org/10.1021/acsnano.2c03062); pmid: [35913128](https://pubmed.ncbi.nlm.nih.gov/35913128/)
34. Z. Li, L. Kong, S. Huang, L. Li, Highly luminescent and ultrastable CsPbBr₃ perovskite quantum dots incorporated into a silica/alumina monolith. *Angew. Chem. Int. Ed.* **56**, 8134–8138 (2017). doi: [10.1002/anie.201703264](https://doi.org/10.1002/anie.201703264); pmid: [28544211](https://pubmed.ncbi.nlm.nih.gov/28544211/)
35. S. Wang *et al.*, Organic polystyrene and inorganic silica double shell protected lead halide perovskite nanocrystals with high emission efficiency and superior stability. *Nano Res.* **16**, 10507–10514 (2023). doi: [10.1007/s12274-023-5489-1](https://doi.org/10.1007/s12274-023-5489-1)
36. Y. Shin *et al.*, Environmentally stable luminescent perovskite nanocrystals passivated and encapsulated by siloxane hybrids enabling reliable color-converted organic light-emitting diodes. *Chem. Eng. J.* **474**, 145889 (2023). doi: [10.1016/j.cej.2023.145889](https://doi.org/10.1016/j.cej.2023.145889)
37. Q. A. Akkerman, G. Rainò, M. V. Kovalenko, L. Manna, Genesis, challenges and opportunities for colloidal lead halide perovskite nanocrystals. *Nat. Mater.* **17**, 394–405 (2018). doi: [10.1038/s41563-018-0018-4](https://doi.org/10.1038/s41563-018-0018-4); pmid: [29459748](https://pubmed.ncbi.nlm.nih.gov/29459748/)
38. S. Yang *et al.*, Stabilizing halide perovskite surfaces for solar cell operation with wide-bandgap lead oxysalts. *Science* **365**, 473–478 (2019). doi: [10.1126/science.aax3294](https://doi.org/10.1126/science.aax3294); pmid: [31371610](https://pubmed.ncbi.nlm.nih.gov/31371610/)
39. N. Yang *et al.*, An in situ cross-linked 1D/3D perovskite heterostructure improves the stability of hybrid perovskite solar cells for over 3000 h operation. *Energy Environ. Sci.* **13**, 4344–4352 (2020). doi: [10.1039/D0EE01736A](https://doi.org/10.1039/D0EE01736A)
40. M. S. Kirschner *et al.*, Photoinduced, reversible phase transitions in all-inorganic perovskite nanocrystals. *Nat. Commun.* **10**, 504 (2019). doi: [10.1038/s41467-019-08362-3](https://doi.org/10.1038/s41467-019-08362-3); pmid: [30700706](https://pubmed.ncbi.nlm.nih.gov/30700706/)
41. H. Tsai *et al.*, Light-induced lattice expansion leads to high-efficiency perovskite solar cells. *Science* **360**, 67–70 (2018). doi: [10.1126/science.aap8671](https://doi.org/10.1126/science.aap8671); pmid: [29622649](https://pubmed.ncbi.nlm.nih.gov/29622649/)
42. B. Zhao *et al.*, Light management for perovskite light-emitting diodes. *Nat. Nanotechnol.* **18**, 981–992 (2023). doi: [10.1038/s41565-023-01482-4](https://doi.org/10.1038/s41565-023-01482-4); pmid: [37653050](https://pubmed.ncbi.nlm.nih.gov/37653050/)

ACKNOWLEDGMENTS

Funding: This research was supported by the Pioneer Research Center Program through the National Research Foundation of Korea (NRF) funded by the Ministry of Science, ICT and Future Planning (RS202500560490, and the Technology Innovation Program (RS-2025-25393382, Development of perovskite nano emissive material for AR/VR near-eye displays) funded by the Ministry of Trade, Industry and Resources (MOTIR, Korea). Q.Z. acknowledges support from Research Institute of Advanced Materials (RIAM), X.W.C. thanks the Agency for Science, Technology and Research (A*STAR, Singapore) for the National Science Scholarship. B.A.I.L. acknowledges the Engineering and Physical Sciences Research Council (EPSRC) and Cambridge Trusts for a PhD studentship. L.D. acknowledges UKRI guarantee funding for Marie Skłodowska-Curie Actions Postdoctoral Fellowships 2022 (EP/Y029429/1). S.D.S. acknowledges the Royal Society and Tata Group (grants UF150033 and URF\RV221026). M.F. and H.J.B. acknowledge funding from the European Union Horizon 2021 research and innovation program (grant agreement 101073045–TADF solutions). **Author contributions:** Conceptualization: Q.Z., T.-W.L. Methods: Q.Z., Y.Z., H.Z., T.-W.L. Investigation: Q.Z., Y.Z., S.P., H.Z., H.-J.S., T.L., J.R., M.-J.S., X.W.C., E.Y., B.A.I.L., S.-J.W., M.F., M.J.K., E.A.K., L.D., J.J., Y.T., J.J.K., H.C., K.Y.J., D.-H.K., W.J.J., J.S.K., H.L., K.L., S.-Y.C., C.B.P., S.K.L., M.K., H.J.B., B.H., A.W., S.D.S., T.-W.L. Visualization: Q.Z., Y.Z., J.R. Funding acquisition: Q.Z., H.J.B., S.D.S., T.-W.L. Writing – original draft: Q.Z. Writing – review & editing: Q.Z., T.-W.L. All authors reviewed and commented on the manuscript. **Competing interests:** T.-W.L. and Q.Z. have filed related patent applications (Korean, PCT, and US patents) based on the findings reported in this work. All other authors declare that they have no competing interests. **Data, code, and materials availability:** All data and details of the synthesis of materials are available in the main text or the supplementary materials. **License information:** Copyright © 2026 the authors, some rights reserved; exclusive licensee American Association for the Advancement of Science. No claim to original US government works. <https://www.science.org/about/science-licenses-journal-article-reuse>. This research was funded in whole or in part by UKRI (EP/Y029429/1), a cOAlition S organization. The author will make the Author Accepted Manuscript (AAM) version available under a CC BY public copyright license.

SUPPLEMENTARY MATERIALS

[science.org/doi/10.1126/science.ady1370](https://www.science.org/doi/10.1126/science.ady1370)
Materials and Methods; Supplementary Text S1 to S11; Figs. S1 to S56; Tables S1 to S16; References (43–116); Movies S1 to S5

Submitted 17 April 2025; accepted 12 November 2025

10.1126/science.ady1370